Revision 1

Gamma-enhancement of reflected light images as a routine method for assessment of compositional heterogeneity in common low-reflectance Fe-bearing minerals

QIAOQIAO ZHU [1], GUIQING XIE [2,*], NIGEL J. COOK [3], CRISTIANA L. CIOBANU [3], HUI WANG[4]

[1] MNR Key Laboratory of Metallogeny and Mineral Assessment, Institute of Mineral Resources, CAGS, Beijing 100037, China

[2] MNR Key Laboratory for Exploration Theory & Technology of Critical Mineral Resources, School of Earth Sciences and Resources, China University of Geosciences, Beijing 100083, China

[3] School of Chemical Engineering, The University of Adelaide, Adelaide, SA 5005, Australia

[4] School of Earth Science and Resources, Chang' an University, Xi' an 710054, China

ABSTRACT

Incorporation of impurity elements into minerals impacts on their physical properties (e.g., reflectance, hardness, and electrical conductivity) but the quantitative relationships between these features and compositional variation remain inadequately constrained. Prior work has shown that gamma-enhancement of reflected light images represents a simple yet powerful tool to assess the compositional heterogeneity of single pyrite crystals as it can enhance subtle differences in reflectance between distinct domains with different minor element concentrations. This study extends the gamma correction method to several other common Fe-bearing minerals, magnetite, garnet, wolframite, and

---

[*] Corresponding author: Dr. Guiqing Xie, E-mail: xieguiqing@cugb.edu.cn

tetrahedrite-tennantite, which all have far lower reflectance than pyrite. Gamma-enhanced optical images reveal clear variations in reflectance that are either systematic with increased minor element concentration as the change in gray value on backscatter electron (BSE) images (in the case of magnetite, garnet, and tetrahedrite-tennantite) or contrasting (as in pyrite), yielding a convincing linkage between reflectance variation and compositional heterogeneity. Reflectance variation is an expression of the distribution of the average effective number of free electrons on the mineral surface that can re-emit light when excited by visible light. Gamma-enhanced images can reveal compositional heterogeneity in minerals such as wolframite where small atomic mass differences between substituting elements (Mn and Fe, in the case of wolframite) are virtually impossible to observe as a variation of gray values on BSE images. Results also demonstrate that Fe-rich domains in these minerals can be expected to have higher reflectance than Fe-poor domains whenever Fe is a major constituent. The greater reflectance is attributed to Fe ions having a greater effective number of free electrons than many other elements (e.g., Co, Ni, Si, Ca, Al, Mg, Mn, and As). The research highlights the utility of gamma correction as an inexpensive tool for routine evaluation of compositional heterogeneity in common Fe-bearing minerals, potentially obviating the necessity of a microbeam platform to correlate textures and composition.

Keywords: Gamma correction; compositional homogeneity; reflectance; magnetite; garnet; wolframite; tetrahedrite-tennantite.

INTRODUCTION

Many minerals display variable compositions and deviate from ideal stoichiometry due to the presence of different levels of impurities induced by solid solution exchange reactions or the presence of discrete nanoscale mineral inclusions (e.g., Craig and Vaughan 1994; Cook et al. 2016; Ciobanu et al. 2019). Such variation can modify the physical features of minerals, such as reflectance, hardness, Raman spectra, and electrical conductivity and may also significantly impact the behavior of a mineral during ore processing (e.g., Craig and Vaughan 1994; Abraitis et al. 2004; Buzatu et al. 2013; Galili et al. 2023). For example, arsenic-rich pyrite exhibits low conductivity, reflectance, and Raman band positions whereas As-poor varieties have relatively higher corresponding features (Saager and Mihálik 1967; Abraitis et al. 2004; Zhu et al. 2020, 2021). In addition, systematic variation of physical features (reflectance, multispectral reflectance, and Raman spectra) have been observed as a function of composition (Craig and Vaughan 1994; López-Benito et al. 2017; Zhu et al. 2020, 2023; Berkh and Rammlmair 2022; Galili et al. 2023). Furthermore, distinct elements in the same mineral may yield varied physical features. In sphalerite, for example, Fe was suggested to affect Raman band positions at ~350 cm^{-1} and 300 cm^{-1} while Cd was assigned to related to a new band position at ~295 cm^{-1} (Babedi et al. 2019). Thus, some specific physical features of minerals have the potential to be used as effective tools to estimate variation in chemical composition without the need for costly and time-consuming electron microprobe analysis. This type of method may thus represent a rapid, user-friendly approach to semi-quantitatively assess the chemical composition of mineral on-site or in outcrop long before any laboratory-based testing is carried out (Jehlička and Culka 2022). Estimates of variation in chemical composition can, in turn, provide critical information on the spatial-temporal evolution of a mineral assemblage or the conditions of its formation or superimposed events. In processing plants, compositional data, especially information on valuable or penalty impurity elements, will assist in prediction and optimization of downstream behavior and metallurgical performance.

Several detailed investigations have suggested that reflectance values of some ore minerals (e.g., pyrite, ilmenite, and galena) are sensitive to compositional variation and have developed rapid method(s) to determine the specific compositions based on their reflectance variation (Saager and Mihalik 1967; Vaughan 1969; Tarkian 1987; Craig and Vaughan 1994). These methods have, however, been in decline since the 1990s due to the lamentable decline in the training and use of reflected light microscopy on a routine basis, as well as two other reasons. Firstly, reflectance variation caused by compositional heterogeneity within minerals is commonly subtle, especially for minerals with relatively low reflectance, and thus can be invisible in conventional polished sections viewed in reflected light, at least without oil immersion (Craig and Vaughan 1994; Craig 2001). Secondly, reflectance data are less definitive than a chemical composition determined by microbeam methods (Stanley 2013). Pačevski (2007) noted that computer-adjusted reflected light images with increased contrast and decreased brightness are useful to observe grain-scale compositional zoning in wolframite. This preliminary research shows an encouraging advantage over back-scattered electron (BSE) imaging in textural characterization of wolframite. Zhu et al. (2021, 2022) noted gamma correction of a reflected light image can enhance reflectance variation between different domains in pyrite and is a robust tool to address the compositional heterogeneity of pyrite at grain scale. This method also belongs to the digital image processing technology and represents an important advance (e.g., non-destructive and reproducible) over traditional techniques (e.g., chemical etching and straining) which were widely used to characterize compositional heterogeneity and ore textures prior to the advent of scanning electron microscope and microprobe analysis as routine characterization techniques (e.g., Ramdohr 1969; Fleet et al. 1993; Gregory et al. 2016, 2019). Gamma correction may be easily conducted on most optical microscopes, requires no special training, and is non-destructive. Recently, we found this method could also be used to routinely characterize ore minerals with relativity lower reflectance and even (semi-)transparent gangue minerals, which are expected to show still subtler reflectance variation induced by the change of composition. Lastly, we note that the general relationship between an increase or decrease in reflectance and compositional variation tied to specific elements has yet to be addressed for many minerals and mineral groups.

There are more than 1000 iron-bearing minerals included in common mineralogy databases (e.g., the webmineral.com Mineralogy Database or the mindat.org database), formed at a wide range of temperatures and pressures and stable in deep mantle, shallow crustal, and surface environments. The reflectance of some major Fe-bearing minerals (e.g., ilmenite, pyrite, and chromite) has been shown to be sensitive to variation in composition (Vaughan 1969; Cervelle et al. 1971; Eales 1980; López-Benito et al. 2017; Zhu et al. 2021). Published reflectance values for these Fe-bearing minerals span a broad range from <10% to >50% and often exhibit variability in reflectance which may be induced by impurity incorporation (Criddle and Stanley 1993; Craig and Vaughan 1994). Therefore, Fe-bearing minerals are ideal candidates to explore relationships between change in reflectance and compositional variation, especially in single mineral grains displaying compositional homogeneity. In this contribution, we use the gamma correction method to investigate the relationship between optical features and compositional variation in four common Fe-bearing minerals: magnetite (~69 wt% Fe); garnet (~19 wt% Fe); wolframite (~7 wt% Fe), and tetrahedrite-tennantite (~1.70 wt% Fe). The results suggest that both solid solution exchange and sub- micron-sized mineral inclusions contribute to the grain-scale compositional heterogeneity causing reflectance variation highlighted in gamma-enhanced reflected images. This study further highlights the potential of gamma-corrected reflected light images as a routine method to assess compositional heterogeneity in common, low reflectance Fe-bearing minerals.

SAMPLING AND METHODOLOGY

The magnetite-bearing sample (JS42) was collected from the Jinshandian Fe skarn deposit, Edong district, eastern China, which occurs at the contact between the 130–127 Ma Jinshandian pluton and Triassic units (Zhu et al. 2015, 2017). Magnetite is the main ore mineral and is associated with phlogopite. Pyrite and anhydrite commonly occur interstitial to magnetite grains or crosscut them. Prior scanning electron microscope (SEM) imaging suggests that some magnetite grains from Jinshandian display two stages of overgrowth although these are hardly visible under reflected light (Fig. 1, Zhu et al. 2019).

The garnet-bearing sample (FJ279-1) was collected from the Fujiashan W-Cu-Mo skarn deposit, Edong district, eastern China, located at the contact between the Late Mesozoic granodiorite porphyry stock (~144 Ma; Ding et al. 2014) and Carboniferous to Triassic carbonate rocks (Ji et al. 2019). Metasomatism is characterized by a thick exoskarn predominantly composed of garnet and minor diopside, vesuvianite, epidote, amphibolite, and wollastonite (Zhu et al. 2023). Compositional heterogeneity of garnet is well preserved and is indicated by a color change from red-brown to light brown or greenish red brown in hand specimens and gray values of BSE images (Fig. 2).

The wolframite-bearing sample (19XLK57) was collected from the Xingluokeng porphyry W deposit, Wuyishan metallogenic belt, eastern China. Ores occur at the roof of a biotite granite porphyry (~152.5 Ma, Wang et al. 2021a). Wolframite and scheelite are the main ore minerals (~1:1) and are distributed as veinlet-disseminated, stockwork, and vein-type mineralization. Two stages of wolframite are recognized, associated with early K-feldspar +scheelite +beryl, and later sulfides (chalcopyrite, sphalerite, and pyrite) +scheelite +Fe-dolomite, respectively (Fig. 3, Wang et al. 2021b).

The sample containing tetrahedrite-tennantite (JJW94) was collected from the Chengmenshan porphyry-skarn Cu deposit, Jiurui district, eastern China. Orebodies occur within the ~146 Ma granodiorite porphyry stock and along the contact zone between the intrusion and marine limestone/dolomite of Permian or Tertiary age (Xu et al. 2021). Copper ores from Chengmenshan are sub-divided into three types according to their location. Sample JJW94 is representative of carbonate-replacement ore occurring within the sedimentary carbonate rocks (Guo et al. 2021). The sample is composed of assimilated sulfides and tetrahedrite-tennantite in a matrix of carbonate minerals. Tetrahedrite-tennantite is associated with chalcopyrite and bornite, and to a less extent, with sphalerite, galena, and pyrite (Fig. 4).

All samples were prepared as 1-inch-diameter polished blocks or polished thin sections. Optical observation, SEM imaging, and electron microprobe analysis (EMPA) were performed at MNR Key

Laboratory of Metallogeny and Mineral Assessment, Institute of Mineral Resources, CAGS. Detailed textural observation on minerals was performed under reflected light in air using an Olympus BX51 Petrographic Microscope. Grains with subtle reflectance variation were chosen to obtain optical digital images at higher magnification (20X, 50X) and conducted gamma correction. Background information on gamma correction can be found in Zhu et al. (2021) and is also described in Online Material Appendix A[1]. The operating procedures using different types of software linked to commonly used optical microscopes can refer to our previous research (Zhu et al. 2021). In this study, gamma-enhancement of reflected light images was refined using the gamma correction function of the NIS-Elements viewer (version 5.21.00) software. The γ parameter is constant at 10 in this study, the same as used by Zhu et al. (2021). The green channel was chosen as the principal color to display the gamma-enhanced images. Green channel intensity of linear profiles on reflected images of magnetite and garnet were measured before and after gamma correction by using the intensity profile function of ZEISS ZEN (version 2.1) software. Following gamma enhancement, the samples were coated with carbon and examined via spot analysis using a JXA-iHP200F Hyper Probe equipped with an energy-dispersive spectrometer (EDS) to evaluate grain-scale compositional heterogeneity. Quantitative mineral compositional data were also obtained using a JXA-iHP200F Hyper Probe microanalyzer. Analytical conditions are described in Online Material Appendix A[1]

RESULTS

---

[1] Deposit item

Variation of reflectance and geochemistry

Mineral textures observable in reflected light images before and after gamma enhancement are illustrated in Figs. 1–4; corresponding EMPA data are listed in Tables 1–4 and plotted in Fig. 5. Magnetite grains (Jinshandian sample) display core and rim textures under reflected light. Core domains (Mag1) are slightly brighter than their rims (Mag2) in reflected light, especially when viewed under high magnification (Fig. 1a). This feature is manifested in gamma-enhanced images which reveal the irregular nature of the domain boundary (Fig. 1b). Optical heterogeneity of some rims is also exposed in the gamma-enhanced images whereby some domains (Mag2D) appear slightly darker than others (Mag2L, Fig. 1b). The differences in reflectance between distinct magnetite domains in the gamma-enhanced images are mirrored by the change in gray values on BSE images (Fig. 1c). EMPA data (Table 1) show that the magnetite rim has greater SiO_2 (1.97–3.45 wt%), CaO (0.73–1.14 wt%), Al_2O_3 (0.69–1.61 wt%), MgO (0.14–1.14 wt%), and K_2O (0.02–0.22 wt%) than the core but is relatively depleted in TiO_2 (<mdl), and V_2O_5, (mostly <mdl) and implicitly, also in calculated FeO^*. The darker domains within the rim (Mag2D) show slightly higher contents of impurities such as Si, Ca, Al, Mg, and K relative to the brighter domains (Mag2L, Fig. 5a). In general, elevated contents of impurities reduce the measured reflectance making such domains darker in both the gamma-enhanced reflected light and BSE images. These features are further supported by qualitative X-ray mapping of Si, Al, and K distributions in magnetite (Fig. 1d–f).

Garnet (Fujiashan sample) shows clear textural and compositional variation (Fig. 2). These garnet grains are characterized by a well-developed oscillatory zoning texture. The zoning is scarcely visible under reflected light (Fig. 2a, d) but is seen clearly on gamma-enhanced and BSE images (Fig. 2b, c, e, f). The variation of brightness in gamma-enhanced images corresponds with the change in gray values in BSE images. EMPA data shows that the garnet of sample FJ279-1 belongs to the grandite series with >90% andradite + grossular endmembers (Table 2). The brighter domains in gamma-enhanced and BSE images contain a higher andradite component (X_{Adr}= ~91 to 98, 26.15–29.66 wt% FeO) than the darker domains (X_{Adr}= ~69 to 81, 21.15–24.35 wt% FeO; Fig. 5b).

Although wolframite, $(\mathrm{Fe,Mn})\mathrm{WO_4}$, a monoclinic mineral, is suggested to display weak bireflectance/pleochroism, the reflectance and color of wolframite in the Xingluokeng specimen shows only faint variation when rotating the microscope stage under plane polarized illumination (Fig. 3a). In contrast, the gamma-enhanced images show clear differences in brightness between different patchy zones (Fig. 3b). Two sub-types of domains are recognized according to the change in brightness on the gamma-enhanced reflected images. Dark domains (Wol1) are observed to be replaced by irregular bright domains (Wol2). Abundant pores are also found at the boundaries between the two domains. However, BSE images show only weak difference in gray values even under very high contrast (Fig. 3c). EMPA data (Table 2) shows that the wolframite in this study features bright domains (Wol2) that have greater mol.% $\mathrm{FeWO_4}$ (41.71–62.03) than the dark domains (Wol1, 18.67–42.86 $\mathrm{FeWO_4}$ mol.%; Fig. 5c). Qualitative X-ray mapping also shows significant differences in Fe and Mn content between these two domains (Fig. 3d, e).

In our case study, the grain margins of tetrahedrite-tennantite are commonly surrounded by chalcopyrite and pyrite (Fig. 4). Extremely weak variation in reflectance is observed under reflected light with the brighter domains appearing light gray with a brownish tint while the darker domain is characterized by a greenish-gray tint (Fig. 4a, d). Gamma-enhanced images show these grains have slightly darker cores (tennantite, Ten) but relatively brighter tetrahedrite rims (Ttr) (Fig. 4b, e), broadly corresponding to the variation in gray values seen on BSE images (Fig. 4c, f). EMPA data confirm differences in composition between tennantite (2.55–3.71 atoms per formula unit (apfu) As, 0.08–1.19 apfu Sb) and tetrahedrite (0.41–1.00 apfu As, 2.86–3.61 apfu Sb) (Fig. 5d; Table 4).

Green channel intensity and composition profiles

Linear profiles of reflected light green channel intensity were acquired for magnetite and garnet before and after gamma correction (Fig. 6). The intensity profile across the Mag1 and Mag2 shows only very small differences prior to gamma correction. However, the Mag2 shows a significant green channel intensity decrease (10–100) while the average intensity of Mag1 retains a similar intensity following gamma correction (Fig. 6a). The gamma-enhanced green channel intensity profile also positively correlates with the variation in Fe content of magnetite but negatively with the total (Si+Ca+Al+Mg) content (Fig. 6b). The intensity profile across oscillatory zoned garnet shows a relatively small variation in green channel intensity (40–172) before gamma correction but this expands to 0–238 after gamma correction (Fig. 6c). The boundaries between individual banded zones are clearly marked by a fluctuation in intensity. Such a major stretch of green channel intensity enhances differences in reflectance that reveal grain-scale compositional zonation. The gamma-enhanced green channel intensity profile is also consistent with the variation of FeO content but negatively correlates with Al_2O_3 content (Fig. 6d). Overall, gamma correction significantly stretches the intensity differences between various compositional domains, resulting in notable reflectance differences in the gamma-enhanced images of both magnetite and garnet.

DISCUSSION

Compositional heterogeneity and reflectance variation of Fe-bearing minerals

Magnetite offers, in principle at least, a series of relatively simple substitution possibilities, even though the mechanisms by which some elements are incorporated are poorly understood or still debated, and where vacancies in either the Fe or O sites are difficult or impossible to verify directly (Nadoll et al. 2014; Deditius et al. 2018; Ciobanu et al. 2019, 2022). The incorporation of common impurity elements (mostly Si and Ca in the case considered here, but also others such as Mg, Al and Ti) will decrease both the reflectance and the average atomic mass of magnetite, as shown in gamma-enhanced images and BSE images, respectively (Fig. 1a–c). The observations may be readily explained in terms of the substitution of Si and Ca, and to a lesser extent Al and Mg, for Fe. Iron content is reduced from a mean of 23.67±0.09 (1σ, n=5) apfu based on a total of 32 oxygen atoms cations in Mag1 to 22.53±0.20 (1σ, n=5) apfu in Mag2L, and just 21.72±0.17 (1σ, n=5) apfu in Mag2D, Fig. 5a; Table 1). This shift decreases the effective number of free electrons (N_{eff}) expected to re-emit light when excited by incident light, increasing the energy required to excite electrons into the conduction band and, consequently, a reduction of reflectance in rim magnetite. This interpretation is further supported by the dataset in the third edition of Quantitative Data File (QDF3; Criddle and Stanley 1993) showing that Si-rich (2.8 wt% SiO_2) magnetite has slightly lower reflectance (~0.7%) than Si-poor magnetite (0.2 wt% SiO_2) at 589 nm in air. Relative differences in reflectance between Mag1 and Mag2 are also clearly revealed by the green channel intensity profiles before and after gamma correction (Fig. 6a). It is worth noting that Mag2 contains detectable K_2O (0.02–0.22 wt%, Table 3), especially in Mag2D (0.11–0.22 wt% K_2O), whereas K is absent in Mag1. The strong correlation between K, Al, and Si may indicate the presence of sub-micron-scale inclusions (phlogopite, for example) contributing to a small decrease in reflectance (Fig. 1d–f). Recent nanoscale research has documented the presence of sub-micron-sized silicate inclusions (e.g., diopside, phlogopite, amphibole, and muscovite) in hydrothermal magnetite, a phenomenon that may be more common than previously thought and could account for aberrant magnetite compositions (e.g., Deditius et al. 2018; Ciobanu et al. 2019, 2022; Cook et al. 2022). The presence of sub-micron-sized mineral inclusions may be an additional factor contributing to variation in reflectance properties in the case considered here.

Garnet, a transparent mineral, reveals the relationship between composition and reflectance variation at the grain scale in our study (Figs. 2, 6c, 6d). Given that Fe has a greater atomic mass than Al, the relative content of Fe and Al is generally reflected by the gray values seen on BSE images, whereby brighter domains have higher Fe (andradite component) and darker domains contain more Al (grossular component) (e.g., Jamtveit et al. 1993; Ciobanu and Cook 2004; Xu et al. 2020). The gamma-enhanced images (Fig. 2b, e) of Fujiashan garnet show similar variation in brightness as the BSE images (Fig. 2c, f), readily explained by difference in electron structures between Al^{3+} and Fe^{3+}, in which Al^{3+} has a larger nucleus and its outermost electrons require higher energy to be excited than is the case for Fe^{3+}. Iron-rich domains in garnet thus have higher reflectance than Al-rich domains and variation in relative brightness simply reflects the relative abundances of Fe^{3+} and Al in simple andradite-grossular solid solutions (Table 2). The green channel intensity profile across compositional domain boundaries can also be used to reveal variation of Fe^{3+} and Al contents at the grain scale (Fig. 6c, d).

The name wolframite refers to intermediate members of the wolframite group, a continuous solid solution between the Fe-rich endmember, ferberite ($FeWO_4$), and the Mn-rich end member hübnerite ($MnWO_4$). Wolframite commonly shows compositional heterogeneity (e.g., Campbell and Petersen 1988; Pačevski 2007) with the Mn/Fe ratio exerting primary control on many physical features, including unit cell dimensions and reflectance (Pačevski 2007). Although reflectance variations are commonly subtle, they can be observed in gamma-enhanced reflected light images (Fig. 3a, b). Burns and Vaughan (1970) noted that Mn^{2+} has an electronic configuration with half-filled 3d orbitals, which leads to reduced covalent bonding and higher-lying Fermi levels than Fe^{2+}, causing the reflectance of MnS and MnS_2 to be lower than for the corresponding iron sulfides (FeS and FeS_2). This phenomenon is consistent with our observation of wolframite, in which Fe-rich domains are brighter than the Mn-rich domains in gamma-enhanced reflected light images (Fig. 3b), even when high-contrast BSE images do not reveal differences in grey values between different domains (Fig. 3c). This is due to the similar mean atomic mass for $FeWO_4$- and $MnWO_4$-rich domains (Neiva 2008). The observation emphasizes how gamma correction can represent a more effective method than BSE imaging to discern compositional variation among domains with only small mean atomic mass differences in certain minerals.

Substituting elements in minerals of the tetrahedrite group, $A_6(B_4C_2)D_4S_{13}$ (Biagioni et al. 2020) may modify the d electrons in the chemical bonding, resulting in reflectance changes (Hall et al. 1974;

Charlat and Lévy 1976). Changes in Ag occupancy in the A and B sites, substituting for Cu, and changing Fe/Zn ratios in the C site would lead to a slight increase in the reflectance whereas substitution of As by Sb in the D site is expected to cause a stronger increase. The significant variation of reflectance related to the D site is attributed to the covalent character of Sb being stronger than As (Hall et al. 1974). Substitution of As by Sb would delocalize electrons, resulting in increasing N_{eff} and reflectance. Differences in the reflectance of tetrahedrite-tennantite cores and rims in our gamma-enhanced images are broadly comparable with the changes in gray shades seen on the BSE images (Fig. 4b–f). The darker core shows higher contents of As and Cu but is relatively depleted in Sb (Table 4; Fig. 5d). A plausible explanation for this is the reflectance decrease induced by substitution of As for Sb overwhelms any increase caused by the change in proportions of Fe and Zn (Hall et al. 1974; Charlat and Lévy 1976). The example of tetrahedrite-tennantite illustrates the complexity introduced by minerals in which multiple substitutions may occur simultaneously in distinct sites and thus masking the relationship between reflectance variation and composition. To this end, greater attention should be paid to the major substitution when linking reflectance variation with compositional change in minerals and mineral groups with complex substitution relationships.

Towards a higher reflectance for Fe-rich domains of common Fe-bearing minerals

The minerals in this study have Fe contents ranging from ~1.7 wt% (tetrahedrite-tennantite), through ~7 wt% (wolframite) and ~19 wt% (garnet), to ~69 wt% (magnetite). All show higher reflectance in Fe-rich domains except for tetrahedrite-tennantite, where Group VA elements (e.g., As and Sb) overwhelmingly determine changes in reflectance behavior (Fig. 5). The reflectance of chromite has been suggested to increase with increasing Fe^{3+} content (Eales 1980; López-Benito et al. 2017). Awadh (2009) noted that the reflectance of Fe-rich (16.96 wt% Fe) sphalerite is slightly higher (~0.9 %) than that of Fe-poor (4.59 wt% Fe) sphalerite at 546 nm in air. Similar results are suggested by recent research on the reflectance of sphalerite (Lai et al. 2023). The reflectance of pyrite was observed to decrease systematically with increasing Ni and/or Co concentrations (Vaughan 1969). Recent research on pyrite shows that unsubstituted Fe-rich domains are brighter than As-rich domains in gamma-enhanced reflected light images (Zhu et al. 2021). In the case of goethite, FeO(OH), Donskoi et al. (2022) noted that varieties rich in Al and/or Si have lower reflectance than those with little or no Al and/or Si. It would therefore appear that Fe-rich domains/grains have higher reflectance in many Fe-bearing minerals (Table 5). This phenomenon is best explained by the difference in electronic structure between Fe ion (Fe^{2+}, Fe^{3+}) and other common constituents (transition metals (Co^{2+}, Ni^{2+}, Mn^{2+}, and Zn^{2+}), alkaline-earth metals (Mg^{2+} and Ca^{2+}), semimetals (Si^{4+} and As^{3+} or As^{-}), and Al^{3+}. The Fe ion has stronger covalent bonding and delocalization of excited t_{2g} electrons than that of the abovementioned elements, resulting in a larger value of the effective number of free electrons that can be excited to re-emit light when visible light is incident on their surface, and hence higher reflectance (Vaughan 1969; Burns and Vaughan 1970). This rule can however be challenged whenever simultaneous substitutions of multiple elements take place, causing divergent changes in reflectance and leading to a mixed or averaged-out result. This is particularly true when Fe is a relatively low-concentration constituent, as in tetrahedrite-tennantite (Fig. 5d).

IMPLICATIONS FOR MINERAL CHARACTERIZATION

Previous research has suggested that the reflectance of minerals may be affected by internal factors such as chemical composition, crystal orientation (anisotropic mineral), and the presence of tiny inclusions as well as external factors including quality of the polished surface, surface tarnishing, grain size (too-small grain will induce errors), light wavelength, immersion medium (air or oil), and the instrumentation and set-up conditions for quantitative measurement (e.g., Criddle 1990; Criddle and Stanley 1993; Craig and Vaughan 1994). Among these, chemical composition and crystal orientation (in anisotropic minerals) may contribute to significant reflectance variation although their interrelationships and the reflectance of many minerals remains unclear or inadequately constrained (e.g., Criddle and Stanley 1993; Craig and Vaughan 1994). The gamma correction method is expected to enhance subtle grain-scale variation in reflectance under reflected light, caused by compositional variation, of Fe-bearing minerals (Figs. 1–4). This method is readily achieved using an optical microscope and digital image processing function of certain software, without destroying the mineral surface and is moreover reproducible, thus representing a significant advantage over traditional chemical etching and staining techniques (Ramdohr 1969; Fleet et al. 1993; Craig 2001; Gregory et al. 2019). Our study demonstrates that gamma correction is a rapid and valid tool for assessing compositional heterogeneity of not only the opaque minerals (magnetite, wolframite, and tetrahedrite-tennantite; Figs. 1, 3, 4) but also transparent minerals such as garnet (Fig. 2) with reflectance as low as ~9 % at 589 nm in air (Criddle 1998). Although internal fractures or crystal defects induce internal reflections that cause color interference and mask some features during gamma correction (Fig. 2b, e), application of the method on (semi-) transparent minerals provides an alternative way to constrain composition variation on epoxy-mounted polished blocks. This type of sample is widely used for quantification of trace element concentration by laser ablation inductively coupled plasma mass spectrometry (LA-ICP-MS) but cannot be observed under transmitted light. The enhanced variation of reflectance for transparent minerals is, however, smaller than that of opaque minerals when using the same gamma values. Prior work also suggested that gamma-enhanced reflected light images can provide sufficient contrast to differentiate crystal boundaries in marcasite (Fig. 3a, b in Zhu et al. 2021). However, the pronounced weak bireflectance for wolframite was insignificant within grains in our study. Variation in reflectance variation induced by composition appeared more significant than by crystallographic orientation. To this extent, the gamma correction method has the potential to assist segmentation and characterization of specific anisotropic minerals with subtle reflectance variation, without requiring stage rotation, use of crossed polars, or the quarter-wave plate (e.g., for hematite; Gomes et al. 2013; Iglesias et al. 2018). A plausible strategy for anisotropic minerals with strong bireflectance is to compare grains with, or rotate the stage of the optical microscope to, a specific crystallographic orientation to minimize the influence of reflectance by crystallographic orientation. Gamma correction may still be useful for constraining the compositional heterogeneity of anisotropic minerals under such a prerequisite or using sections with specific crystallographic orientations.

Gamma-enhanced variation in the relative reflectance can be either the same as (e.g., tetrahedrite-tennantite, garnet, and magnetite), or contrasting with (e.g., pyrite, Zhu et al. 2021), the change in gray values seen on BSE images, which vary as a function of mean atomic mass (Paterson et al. 1989; Craig et al. 1998; Craig 2001). These relationships represent an implicit link between reflectance variation and compositional variation. The intensity profile of the signal light channel in the gamma-enhanced reflected light image is thus directly comparable to the composition profile although it is an aggregated response to the increase and decrease of reflectance caused by individual element substitutions and/or sub-micron-sized mineral inclusions (Fig. 6). Given that multiple elements are commonly located in the same crystal sites in many complex solid solution series (e.g., spinel, garnet, tetrahedrite-tennantite), reflectance variation in the gamma-enhanced image is a cumulative effect reflecting the change in the average effective number of free electrons of the mineral surface. The substitution-induced Fe-rich domains are expected to have higher reflectance than Fe-poor domains whenever Fe is a major constituent (Fig. 5a–c). The gamma-enhanced images of certain minerals may be more perspicuous than the respective BSE images whenever the differences in atomic mass between substituted and substituting elements is too small to cause significant gray value variation (e.g., Mn for Fe in wolframite, Co and/or Ni for Fe in pyrite; Fig. 3b, c; Vaughan 1969; Craig et al. 1998). Further applications are thus expected to be found in mineral/porosity segmentation and texture classification, which are of fundamental importance in automated and quantitative optical mineral characterization. It could be used, for example, to address other economically important iron-oxides and hydroxides (e.g., goethite, hematite, magnetite) that have complex, varying chemical compositions that cannot be reliably constrained by SEM-EDS and other traditional methods alone (Iglesias et al. 2018; López-Benito et al. 2020; Donskoi et al. 2022). These minerals and the porosity between their particles are expected to display marked differences in gray levels and therefore easy to identify and segment automatically if the gamma value and acquisition conditions are kept stable (Iglesias et al. 2018; Donskoi et al. 2022). The reproducibility of this process is one key advantage of using automatic acquisition in preference to a human operator (Iglesias et al. 2018). Recent research has highlighted the potential of coupled cathodoluminescence (CL) spectra and SEM for characterizing the mineralogy, chemical composition, and crystal properties of goethite, hematite, and magnetite (Galili et al. 2023). This no-destructive method relies on the SEM instrument to locate target minerals and is strongly challenged by the interface of nearby high-luminescence minerals (e.g., quartz and carbonate minerals). Gamma correction is low-cost and easy to conduct although it lacks a comparable range of magnification and spatial resolution. Gamma correction nevertheless represents an alternative, optical-based technique that can be used instead of or complement BSE imaging.

In general, gamma correction can be used as a routine method to assess compositional heterogeneity for certain Fe-bearing opaque and even transparent minerals prior to quantitative analysis. It can also provide robust textural evidence for minerals that have undergone multiple stages of overgrowth or display variations in growth habit from core to rim, in turn indicating an evolution of hydrothermal fluid or magma (e.g., Murowchick and Barnes 1987; Craig 2001; Ciobanu and Cook 2004). Gamma correction may therefore open a broad range of innovative applications in (automated) mineral characterization, mineral exploration, and metal recovery.

ACKNOWLEDGEMENTS

We acknowledge Drs. Zhenyu Chen and Xiaodan Chen (Institute of Mineral Resources, CAGS) for assistance with scanning electron microscope operation and electron probe microanalysis. Special thanks are due to Senior Engineers Qingyue Hu, Shanggang Jin, and Ketao Wei (First Geological Team of Hubei Geological Bureau), and

Dr. Yunhao Ji (CUGB) for assistance with fieldwork and sample collection. This research was funded by the National Natural Science Foundation of China (41925011, 92162217), and Basic Scientific Research Operation Cost of State-Leveled Public Welfare Scientific Research Courtyard (KK2212). Two reviewers and Associate Editor Callum Hetherington are thanked for their valuable comments on our work that helped us improve clarity.

REFERENCES CITED

Abraitis, P.K., Pattrick, R.A.D., and Vaughan, D.J. (2004) Variations in the compositional, textural and electrical properties of natural pyrite: A review. International Journal of Mineral Processing, 74, 41–59.

Awadh, S.M. (2009) Iron content variations in sphalerite and their effects on reflectance and internal reflections under reflected light. Arabian Journal of Geosciences, 2, 139–142.

Babedi, L., Von Der Heyden, B.P., Neethling, P.H., and Tadie, M. (2019) The effect of Cd-substitution on the Raman vibrational characteristics of sphalerite. Vibrational Spectroscopy, 105, 102968.

Berkh, K., and Rammlmair, D. (2022) The effect of Co substitution on the Raman spectra of pyrite: potential as an assaying tool. European Journal of Mineralogy, 34, 259–274.

Biagioni, C., George, L. L., Cook, N. J., Makovicky, E., Moëlo, Y., Pasero, M., Sejkora, J., Stanley, C.J., Welch, M.D., and Bosi, F. (2020) The tetrahedrite group: Nomenclature and classification. American Mineralogist, 105, 109–122.

Burns, R.G., and Vaughan, D.J. (1970) Interpretation of the reflectivity behavior of ore minerals. American Mineralogist, 55, 1576–1586.

Buzatu, A., Buzgar, N., Damian, G., Vasilache, V., and Apopei, A.I. (2013) The determination of the Fe content in natural sphalerites by means of Raman spectroscopy. Vibrational Spectroscopy, 68, 220–224.

Campbell, A., and Petersen, U. (1988) Chemical zoning in wolframite from San Cristobal, Peru. Mineralium Deposita, 23, 132–137.

Cervelle, B., Levy, C., and Caye, R. (1971) Dosage rapide du magnésium dans les ilménites par microréflectométrie. Mineralium Deposita, 6, 34–40.

Charlat, M., and Lévy, C. (1976) Influence des principales substitutions sur les propriétés optiques dans la série tennantite-tétraédrite. Bull. Soc. française Minéral. Cristallograph, 99, 29–37.

Ciobanu, C. L., Verdugo-Ihl, M. R., Cook, N. J., Ehrig, K., Slattery, A., and Courtney-Davies, L. (2022). Ferro-tschermakite with polysomatic chain-width disorder identified in silician magnetite from Wirrda Well, South Australia: A HAADF STEM study. American Mineralogist, 107, 765–777.

Ciobanu, C.L., and Cook, N.J. (2004) Skarn textures and a case study: the Ocna de Fier-Dognecea orefield, Banat, Romania. Ore Geology Reviews, 24, 315–370.

Ciobanu, C.L., Verdugo-Ihl, M.R., Slattery, A., Cook, N.J., Ehrig, K., Courtney-Davies, L., and Wade, B.P. (2019) Silician magnetite: Si–Fe-Nanoprecipitates and other mineral inclusions in magnetite from the Olympic Dam deposit, South Australia. Minerals, 9, 311.

Cook, N.J., Ciobanu, C.L., Ehrig, K., Slattery, A.D., and Gilbert, S.E. (2022) Micron- to atomic-scale investigation of rare earth elements in iron oxides. Frontiers in Earth Science, 10, 967189.

Cook, N.J, Ciobanu, C.L., George, L., Zhu, Z.Y., Wade, B., and Ehrig, K. (2016) Trace element analysis of minerals in magmatic-hydrothermal ores by laser ablation inductively-coupled plasma mass spectrometry: Approaches and opportunities. Minerals, 6, 111.

Craig, J.R., (2001) Ore-mineral textures and the tales they tell. The Canadian Mineralogist, 39, 937–956.

Craig, J.R., and Vaughan, D.J. (1994) Ore Microscopy and Ore Petrography, 2nd ed., 434 p. John Wiley and Sons, Inc., New York.

Craig, J.R., Vokes, F.M., and Solberg, T.N. (1998) Pyrite: Physical and chemical textures. Mineralium Deposita, 34, 82–101.

Criddle, A. J., Jambor, J. L., and Vaughan, D. J. (1990) Microscope-photometry, reflectance measurement, and quantitative color. In: J.L. Jambor and D.J. Vaughan, Eds., Advanced Microscopic Studies of Ore Minerals, 17, 135–169.

Criddle, A.J. (1998) Ore microscopy and photometry (1890–1998). In: L. Cabri and D.J. Vaughan, Eds., Modern Approaches to Ore and Environmental Mineralogy, 27, 1–74.

Criddle, A.J., and Stanley, C.J. (1993) Quantitative Data File for Ore Minerals, 3rd ed., 635 p. Chapman and Hall / Natural History Museum, London.

Deditius, A.P., Reich, M., Simon, A.C., Suvorova, A., Knipping, J., Roberts, M.P., Rubanov, S., Dodd, A., and Saunders, M. (2018) Nanogeochemistry of hydrothermal magnetite. Contributions to Mineralogy and Petrology, 173, 46.

Ding, L.X., Huang, G.C., and Xia, J.L. (2014) Petrogenesis of the Longjiaoshan-Fujiashan porphyritic intrusion in southeastern Hubei Province and implications for Cu-W mineralization. Acta Geologica Sinica, 88, 1513–1527 (in Chinese with English abstract).

Donskoi, E., Manuel, J. R., Hapugoda, S., Poliakov, A., Raynlyn, T., Austin, P., and Peterson, M. (2022) Automated optical image analysis of goethitic iron ores. Mineral Processing and Extractive Metallurgy, 131, 14–24.

Eales, H.V. (1980) The application of reflectivity measurements to the study of chromiferous spinels. The Canadian Mineralogist, 18, 17–23.

Fleet, M.E., Chryssoulis, S.L., MacLean, P.J., Davidson, R. and Weisener, C.G. (1993) Arsenian pyrite from gold deposits; Au and As distribution investigated by SIMS and EMP, and color staining and surface oxidation by XPS and LIMS. The Canadian Mineralogist, 31, 1–17.

Galili, N., Kaplan-Ashiri, I., and Halevy, I. (2023) Cathodoluminescence of iron oxides and oxyhydroxides. American Mineralogist, 108, 1436–1448.

George, L.L., Biagioni, C., D'Orazio, M., and Cook, N.J. (2018) Textural and trace element evolution of pyrite during greenschist facies metamorphic recrystallization in the southern Apuan Alps (Tuscany, Italy): Influence on the formation of Tl-rich sulfosalt melt. Ore Geology Reviews, 102, 59–105.

George, L.L., Biagioni, C., Lepore, G.O., Lacalamita, M., Agrosì, G., Capitani, G.C., Bonaccorsi, E., and d'Acapito, F. (2019) The speciation of thallium in (Tl, Sb, As)-rich pyrite. Ore Geology Reviews, 107, 364–380.

Gomes, O.D.M., Iglesias, J.C.A., Paciornik, S., and Vieira, M.B. (2013) Classification of hematite types in iron ores through circularly polarized light microscopy and image analysis. Minerals Engineering, 52, 191–197.

Gregory, D.D., Large, R.R., Bath, A.B., Steadman, J.A., Wu, S., Danyushevsky, L., Bull, S.W., Holden, P., and Ireland, T.R. (2016) Trace element content of pyrite from the Kapai Slate, St. Ives Gold District, Western Australia. Economic Geology, 111, 1297–1320.

Gregory, D.D., Mukherjee, I., Olson, S.L., Large, R.R., Danyushevsky, L.V., Stepanov, A.S., Avila, J.N., Cliff, J., Ireland, T.R., Raiswell, R., and others (2019) The formation mechanisms of sedimentary pyrite nodules determined by trace element and sulfur isotope microanalysis. Geochimica et Cosmochimica Acta, 259, 53–68.

Guo, X.Z., Zhou, T.F., Wang, F.Y., Ye, S.Z., and Feng, D.S. (2021) Study of occurrence states and precipitation mechanism of tellurium in Chengmenshan porphyry-skarn deposit from the Middle-Lower Yangtze River Valley Metallogenic Belt. Acta Petrologica Sinica, 37, 2723–2742 (in Chinese with English abstract).

Hall, A.J., Cervelle, B., Lévy, C. (1974) The effect of substitution of Cu by Zn, Fe and Ag on the optical properties of synthetic tetrahedrite, $Cu_{12}Sb_4S_{13}$. Bulletin de Minéralogie, 97, 18–26.

Iglesias, J.C.Á., Augusto, K.S., Gomes, O.D.F.M., Domingues, A.L.A., Vieira, M.B., Casagrande, C., and Paciornik, S. (2018) Automatic characterization of iron ore by digital microscopy and image analysis. Journal of Materials Research and Technology, 7, 376–380.

Jamtveit, B., Wogelius, R.A., and Fraser, D.G. (1993) Zonation patterns of skarn garnets: Records of hydrothermal system evolution. Geology, 21, 113–116.

Jehlička, J., and Culka, A. (2022) Critical evaluation of portable Raman spectrometers: From rock outcrops and planetary analogs to cultural heritage–A review. Analytica Chimica Acta, 1209, 339027.

Ji, Y.H., Xie, G.Q., Zhu, Q.Q., Sun, X.F., and Li, X.H. (2019) Influence of carbonaceous strata on skarn tungsten deposits: A case study of Fujiashan deposit in eastern Hubei Province. Mineral Deposits, 38, 917–934 (in Chinese with English abstract).

Lai, X., Chen, C.H., Yang, Y.L., Liu, S.Y., Li, Y., Wang, J.X., Song, Z.J., Gu, Y., Chen, X.J., and Huang, X.D. (2023) Constraints on Metallogenic Temperature and Mineralization Style from Reflection Color of Sphalerite. Ore Geology Reviews, 161, 105634.

López-Benito, A., Catalina, J. C., Alarcón, D., Grunwald, Ú., Romero, P., and Castroviejo, R. (2020). Automated ore microscopy based on multispectral measurements of specular reflectance. I–A comparative study of some supervised classification techniques. Minerals Engineering, 146, 106136.

López-Benito, A., Gervilla, F., Catalina, J.C., and Castroviejo, R. (2017) Chromite typology and composition characterized through multispectral specular reflectance. Ore Geology Reviews, 89, 132–142.

Murowchick, J.B., and Barnes, H.L. (1987) Effects of temperature and degree of supersaturation on pyrite morphology. American Mineralogist, 72, 1241–1250.

Nadoll, P., Angerer, T., Mauk, J.L., French, D., and Walshe, J. (2014) The chemistry of hydrothermal magnetite: a review. Ore Geology Reviews, 61, 1–32.

Neiva, A. (2008) Geochemistry of cassiterite and wolframite from tin and tungsten quartz veins in Portugal. Ore Geology Reviews, 33, 221–238.

Pačevski, A., Götzinger, M., Dimitrijević, R. and Cvetković, L. (2007) Oscillatory zoning in wolframite from Osanica, near Bor, Serbia. Neues Jahrbuch für Mineralogie-Abhandlungen, Journal of Mineralogy and Geochemistry, 184, 151–160.

Paterson, B.A., Stephens, W.E., and Herd, D.A. (1989) Zoning in granitoid accessory minerals as revealed by backscattered electron imagery. Mineralogical Magazine, 53, 55–61.

Ramdohr, P. (1969) The Ore Minerals and Their Intergrowths,1st ed., 1174 p. Pergamon Press, London.

Saager, R., and Mihalik, P. (1967) Two varieties of pyrite from the Basal Reef of the Witwatersrand System. Economic Geology, 62, 719–731.

Stanley, C.J. (2013) Quantitative reflected light microscopy: A searchable web-based database of the four COM wavelengths. https://www.mindat.org/article.php/1829/Quantitative+reflected+light+microscopy%

3A+A+searchable+web-based+database+of+the+ (accessed Jan 9, 2024).

Tarkian, M. (1987) Compositional variations and reflectance of the common platinum-group minerals. Mineralogy and Petrology, 36, 169–190.

Vaughan, D.J. (1969) Zonal variation in bravoite. American Mineralogist, 54, 1075–1083.

Vaughan, D.J. (1978) The interpretation and prediction of the properties of opaque minerals from crystal chemical models. Bulletin de Minéralogie, 101, 484–497.

Wang, H, Feng, CY, Li, R.X., Li, C., Zhao, C., Chen, X., and Wang, G.H. (2021b) Ore-forming mechanism and fluid evolution processes of the Xingluokeng tungsten deposit, western Fujian Province: Constraints form in-situ trace elemental and Sr isotopic analyses of scheelite. Acta Petrologica Sinica, 37, 698–716 (in Chinese with English abstract).

Wang, H., Feng, C.Y., Li, R.X., Zhao, C., Liu, P., Wang, G.H., and Hao, Y.J. (2021a) Petrogenesis of the Xingluokeng W-bearing granitic stock, western Fujian Province, SE China and its genetic link to W mineralization. Ore Geology Reviews, 132, 103987.

Xu, J., Ciobanu, C.L., Cook, N.J., Zheng, Y.Y., Sun, X., and Wade, B.P. (2016) Skarn formation and trace elements in garnet and associated minerals from Zhibula copper deposit, Gangdese Belt, southern Tibet. Lithos, 262, 213–231.

Xu, Y.M., Jiang, S.Y., and Zhu, J.X. (2021) Factors controlling the formation of large porphyry Cu deposits: A case study from the Jiurui ore district of Middle-Lower Yangtze River Metallogenic Belt using in situ zircon and apatite chemistry from syn-mineralization intrusions. Ore Geology Reviews, 133, 104082.

Zhu Q.Q., Xie G.Q., and Li W. (2019) Superposition mechanism of Fe enrichment in skarn deposits of Edong district: Constrains from magnetite texture and ore grade data. Acta Petrologica Sinica, 35, 3703–3720 (in Chinese with English abstract).

Zhu, Q.Q., Cook, N. J., Xie, G.Q., Ciobanu, C. L., Gilbert, S. E., Wade, B., and Xu, J. (2022) Textural and geochemical analysis of celestine and sulfides constrain Sr-(Pb-Zn) mineralization in the Shizilishan deposit, eastern China. Ore Geology Reviews, 144, 104814.

Zhu, Q.Q., Cook, N.J., Xie, G.Q., Ciobanu, C.L., Jian, W., Wade, B.P., and Xu, J. (2021) Gamma-enhancement of reflected light images: A rapid, effective tool for assessment of compositional heterogeneity in pyrite. American Mineralogist, 106, 497–505.

Zhu, Q.Q., Cook, N.J., Xie, G.Q., Ciobanu, C.L., and Ji Y.H. (2023) Determination of skarn garnet compositions using Raman spectroscopy. Journal of Raman Spectroscopy. 54, 217–224.

Zhu, Q.Q., Cook, N.J., Xie, G.Q., Wade, B.P., and Ciobanu, C.L. (2020) Arsenic-induced downshift of Raman band positions for pyrite. Economic Geology, 115, 1589–1600.

Zhu, Q.Q., Xie, G.Q., Mao, J.W., Hou, K.J., Sun, J.F., and Jiang, Z.S. (2017) Formation of the Jinshandian Fe skarn ore field in the Edong district, eastern China: constraints from U-Pb and ^{40}Ar/ ^{39}Ar geochronology. Ore Geology Reviews, 86, 1–20.

Figure captions

FIGURE 1. Reflected light (**a**), gamma-enhanced (**b**), back-scattered electron (BSE) images (**c**), and qualitative X-ray element maps (**d**, **e**, and **f**) showing textures and compositional heterogeneity in magnetite (Mag) from the Jinshandian deposit. Rounded Mag1 (light gray) is preserved as a core domain within Mag2 (gray) as demonstrated in the reflected light (**a**), gamma-enhanced (**b**), and BSE (**c**) images. The curved boundary

between the core domain (Mag1) and rim (Mag2) is marked by white dashed lines in the gamma-enhanced images (**b**). Boundaries between dark (Mag2D) and bright (Mag2L) domains in the rim are demonstrated in the gamma-enhanced (marked by white dashed arrow in inset on b) and BSE (**c**) images but are only faintly seen in reflected light (**a**). Compositional heterogeneity in Mag2 and differences between Mag1 and Mag2 are revealed by variation in the contents of Si (**d**), Al (**e**), and K (**f**).

FIGURE 2. Reflected light (**a** and **d**), gamma-enhanced (**b** and **e**), and BSE images (**c** and **f**) showing textural and compositional heterogeneity in andradite-grossular garnet (Grt) from the Fujiashan deposit. Variation in reflectance of the garnet is hardly visible in reflected light but a clear oscillatory zoning texture is seen on both gamma-enhanced (**b** and **e**) and BSE images (**c** and **f**). Note the internal fractures or crystal defects induced by internal reflection may cause color interference and mask some features during gamma correction (marked by white arrows on **d** and **e**).

FIGURE 3. Reflected light (**a**), gamma-enhanced (**b**), BSE images (**c**), and qualitative X-ray maps (**d**–**f**) showing textural and compositional heterogeneity in wolframite (Xingluokeng sample). Reflectance variation in wolframite (Wol) is hardly visible in reflected light (**a**) and high-contrast BSE images (**c**) but is clearly demonstrated in the gamma-enhanced image (**b**). Compositional differences between Wol1 and Wol2 are revealed by variation in the contents of Fe (**d**) and Mn (**e**) while Nb (**f**) shows no difference between the two domains. Weak brownish internal reflection is shining through and marked by the white arrow in (**a**). The presence of abundant micro-sized pores near the boundary between Wol1 and Wol2 may indicate replacement as shown in the gamma-enhanced image (**b**).

FIGURE 4. Reflected light (**a** and **d**), gamma-enhanced (**b** and **e**), and BSE images (**c** and **f**) showing the texture

and compositional heterogeneity of tetrahedrite-tennantite (Chengmenshan sample). Tetrahedrite-tennantite shows a very weak variation in reflectance and color (from greenish gray to gray with a brownish tint) (**a**, **b**). Gamma-enhanced reflected images show clear reflectance variation (**b**, **e**) and the brightness correlates well with the gray values of the BSE images (**c**, **f**). Boundaries between core tennantite (Ten) and rim tetrahedrite (Ttr) are marked by white dashed lines on the gamma-enhanced images (**b** and **e**). Abbreviations: Ccp–chalcopyrite; Py–pyrite; Ten–tennantite; Ttr–tetrahedrite.

FIGURE 5. Binary correlation plots from EMPA data showing compositional heterogeneity in magnetite (**a**), garnet (**b**), wolframite (**c**), and tetrahedrite-tennantite (**d**). Chemical compositions of magnetite and tetrahedrite-tennantite were calculated based on normalization to 32 O atoms and 29 total atoms, respectively. Arrows indicate how brightness changes with mineral composition when observed under reflected light. Abbreviations: Mag–magnetite; Grt–garnet; Wol–wolframite; Ten–tennantite; Ttr–tetrahedrite.

FIGURE 6. Green channel intensity profiles of reflected light images (**a**, **c**) and compositional profiles (**b**, **d**) for magnetite and garnet at the grain scale. Gray and black lines are intensity profiles before and after gamma enhancement, respectively.

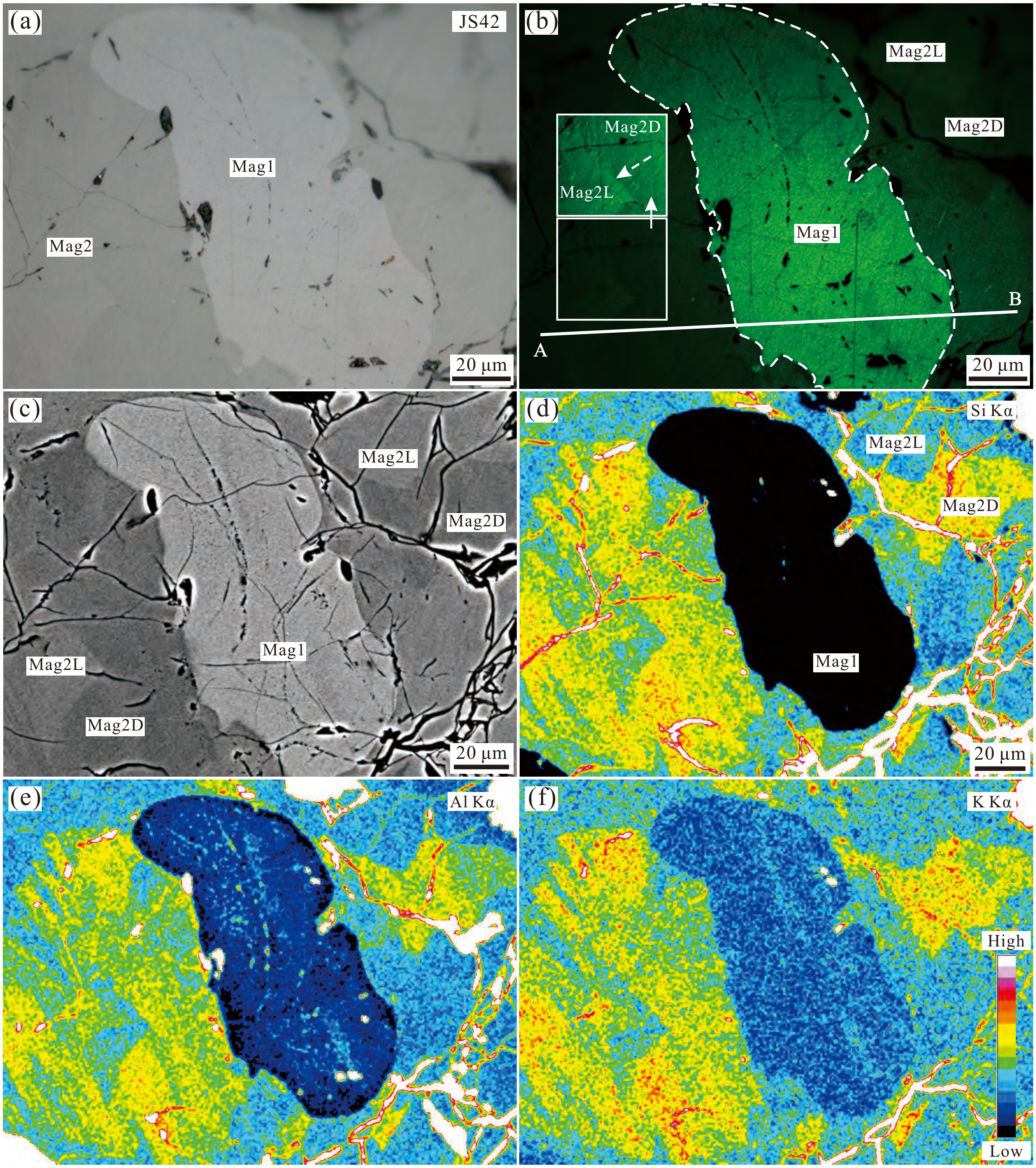
(a)
JS42
Mag1
Mag2
20 μm
(b)
Mag2L
Mag2D
Mag2D
Mag2L
Mag1
A
B
20 μm
(c)
Mag2L
Mag2D
Mag1
Mag2L
Mag2D
20 μm
(d)
Si Kα
Mag2L
Mag2D
Mag1
20 μm
(e)
Al Kα
(f)
K Kα
High
Low

Figure 1

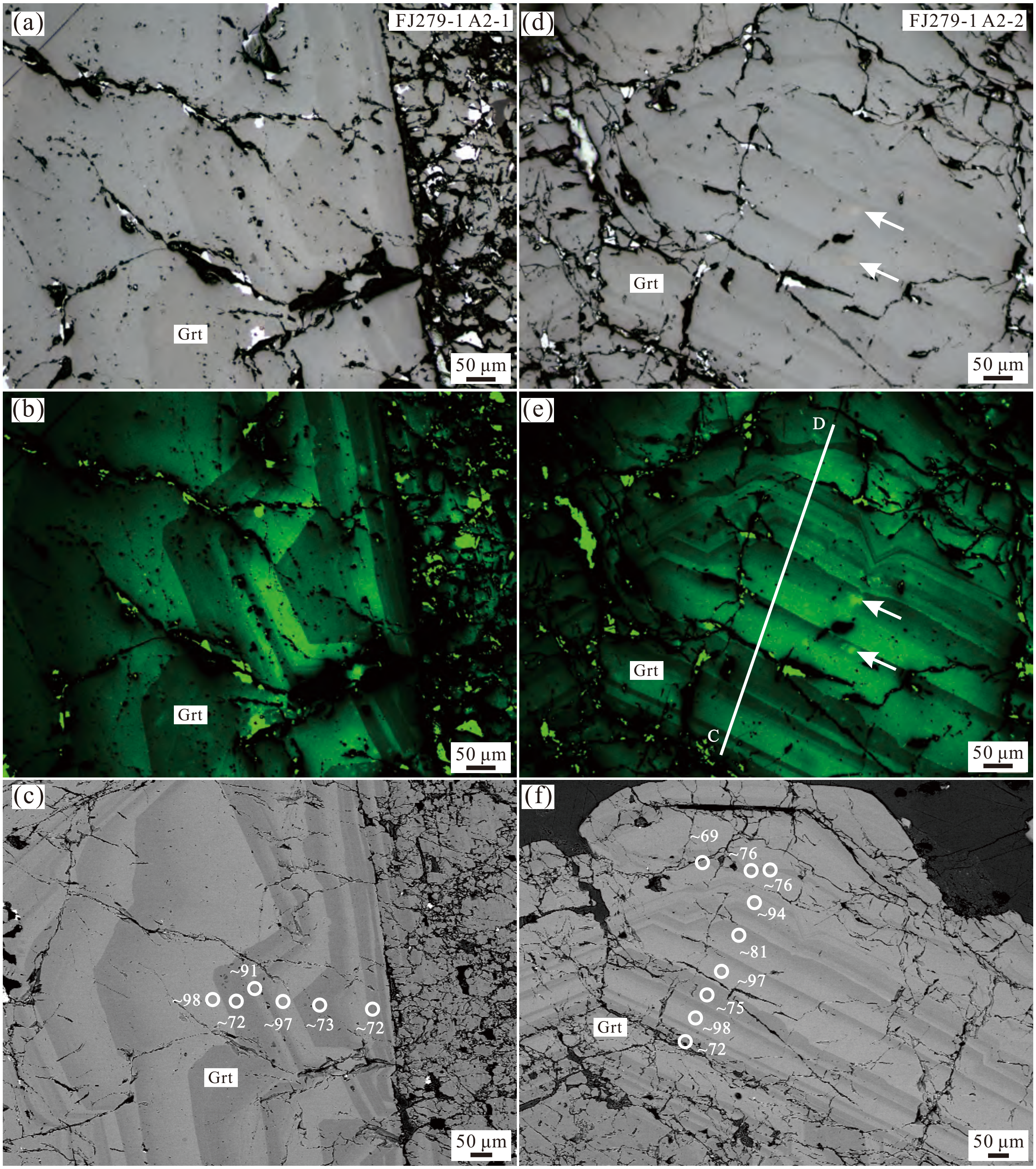
(a)
FJ279-1 A2-1
Grt
50 μm
(b)
Grt
50 μm
(c)
~91
~98
~72
~97
~73
~72
Grt
50 μm
(d)
FJ279-1 A2-2
Grt
50 μm
(e)
D
Grt
C
50 μm
(f)
~69
~76
~76
~94
~81
~97
~75
~98
~72
Grt
50 μm

Figure 2

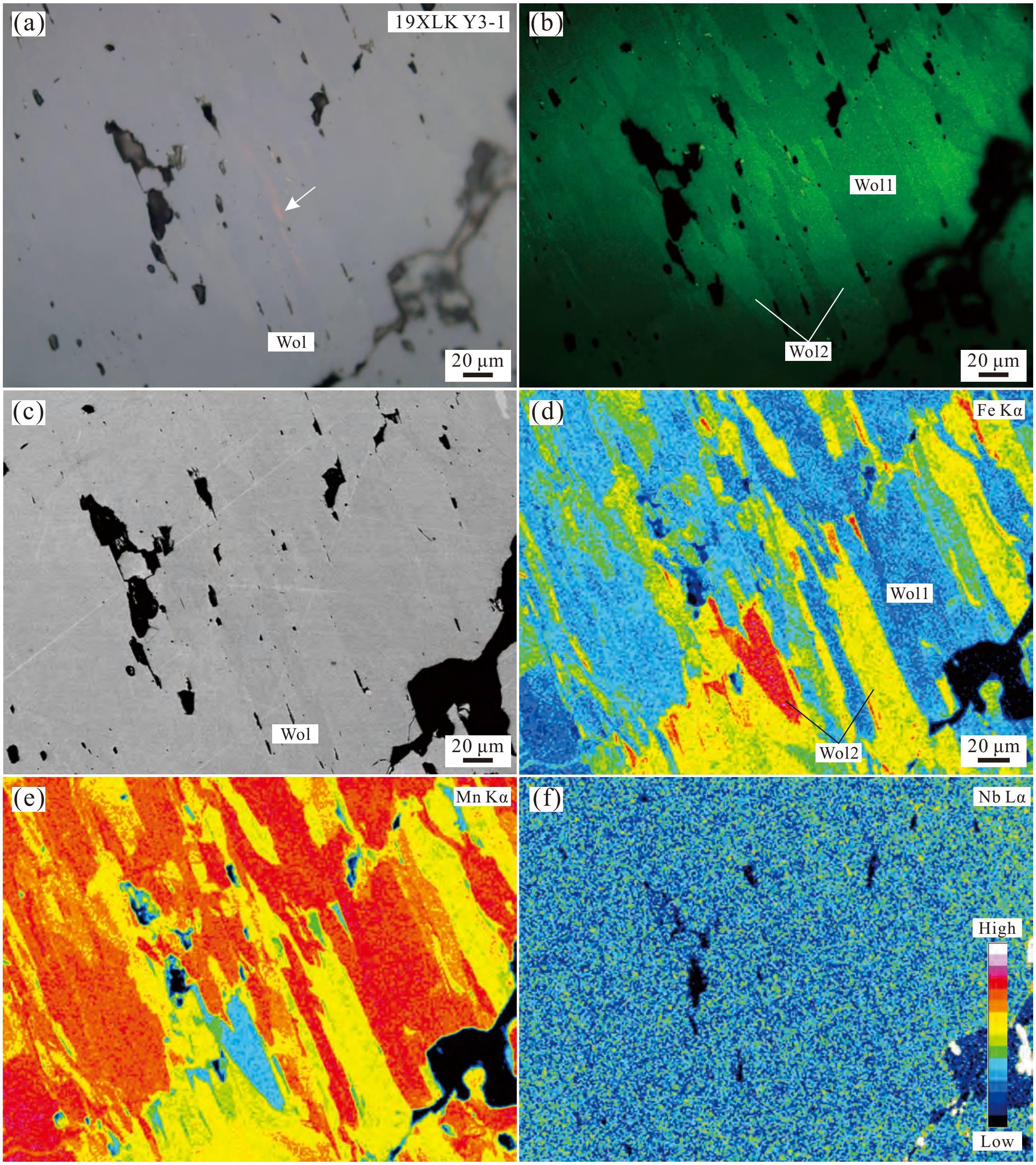
(a)
19XLK Y3-1
Wol
20 μm
(b)
Wol1
Wol2
20 μm
(c)
Wol
20 μm
(d)
Fe Kα
Wol1
Wol2
20 μm
(e)
Mn Kα
(f)
Nb Lα
High
Low

Figure 3

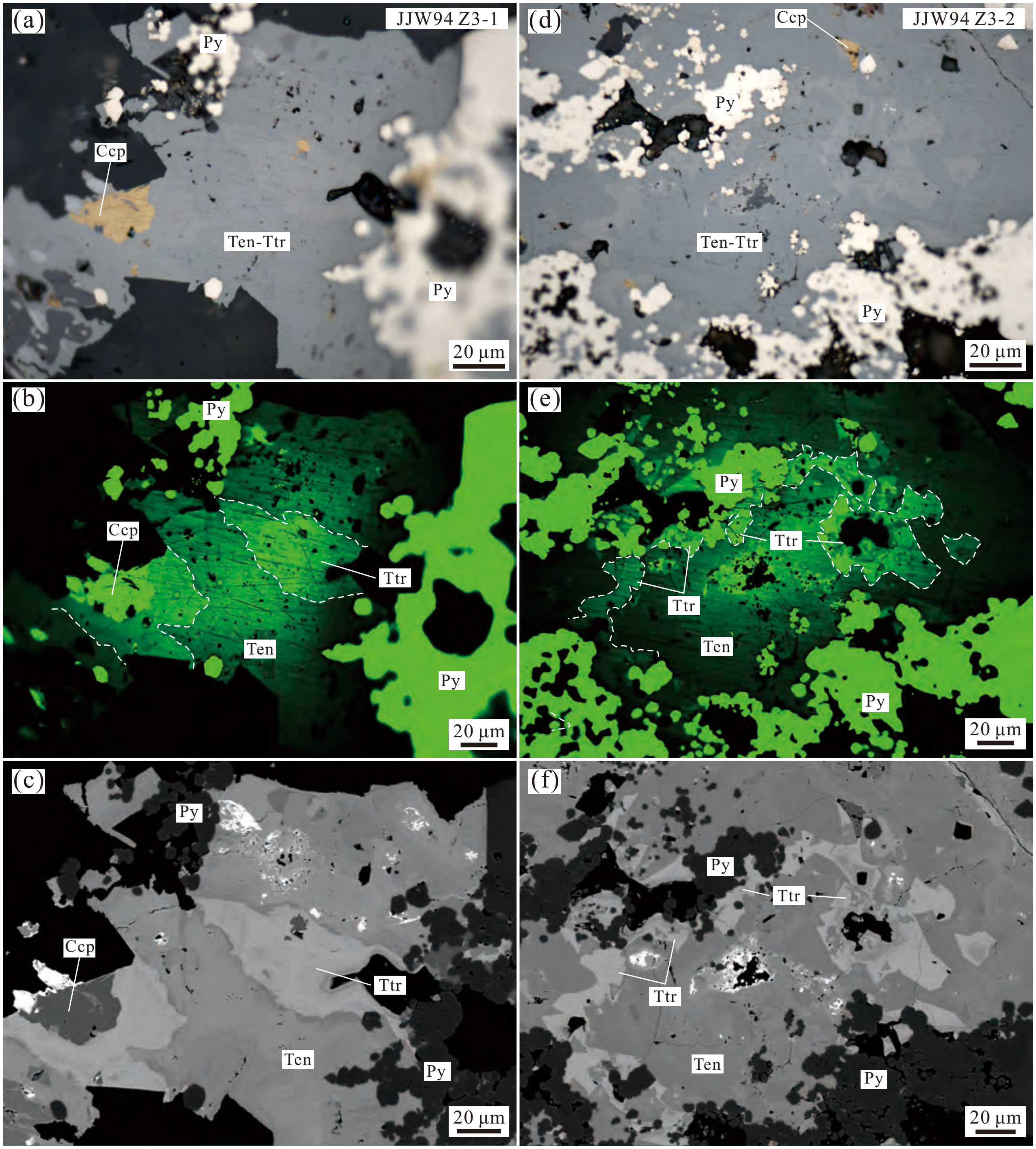
(a)
JJW94 Z3-1
Py
Ccp
Ten-Ttr
Py
20 µm
(d)
Ccp
JJW94 Z3-2
Py
Ten-Ttr
Py
20 µm
(b)
Py
Ccp
Ttr
Ten
Py
20 µm
(e)
Py
Ttr
Ttr
Ten
Py
20 µm
(c)
Py
Ccp
Ttr
Ten
Py
20 µm
(f)
Py
Ttr
Ttr
Ten
Py
20 µm

Figure 4

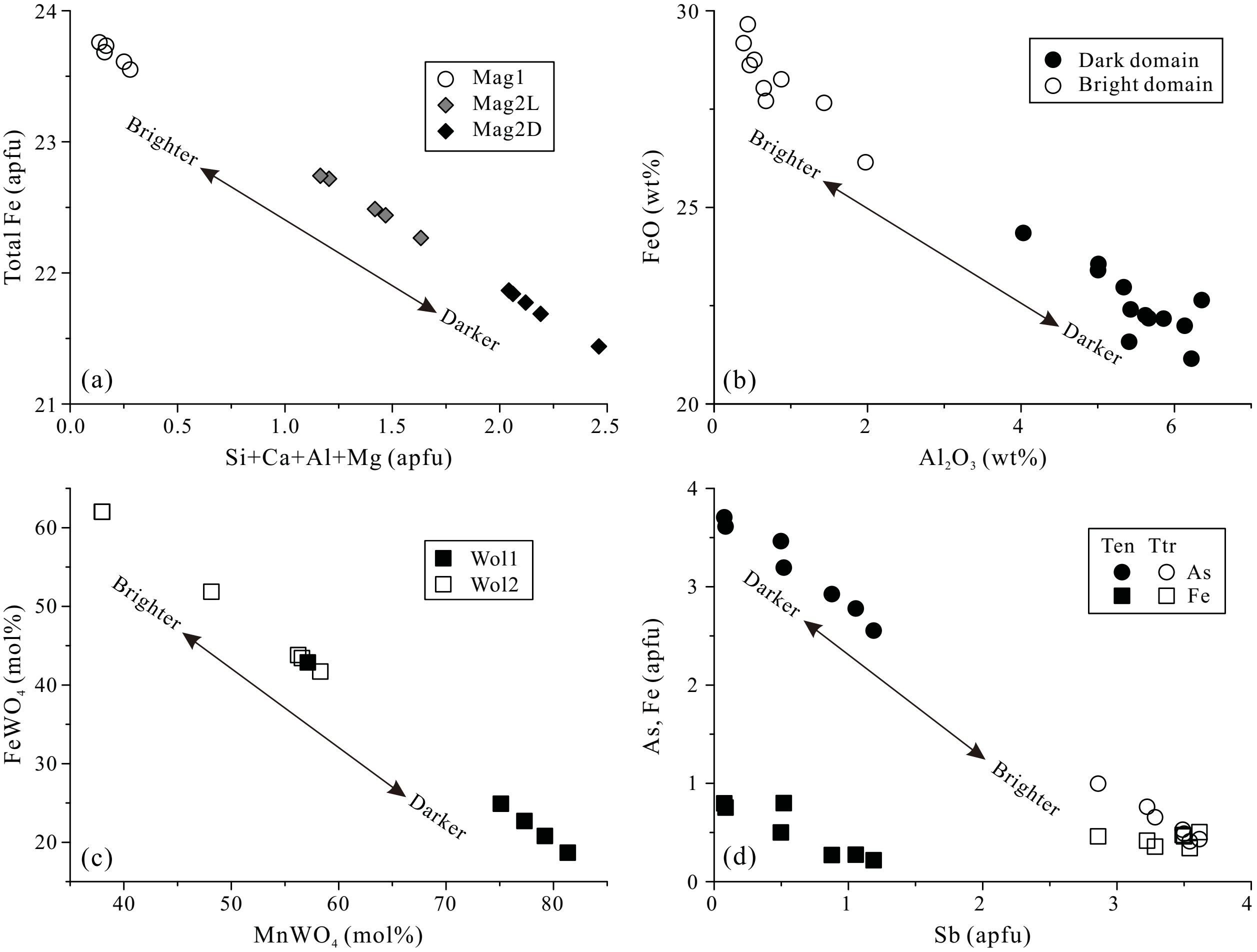
(a)
Total Fe (apfu)
Si+Ca+Al+Mg (apfu)
24
23
22
21
0.0
0.5
1.0
1.5
2.0
2.5
Mag1
Mag2L
Mag2D
Brighter
Darker
(b)
FeO (wt%)
Al_2O_3 (wt%)
30
25
20
0
2
4
6
Dark domain
Bright domain
Brighter
Darker
(c)
$FeWO_4$ (mol%)
$MnWO_4$ (mol%)
60
50
40
30
20
40
50
60
70
80
Wol1
Wol2
Brighter
Darker
(d)
As, Fe (apfu)
Sb (apfu)
4
3
2
1
0
0
1
2
3
4
Ten Ttr
As
Fe
Darker
Brighter

Figure 5

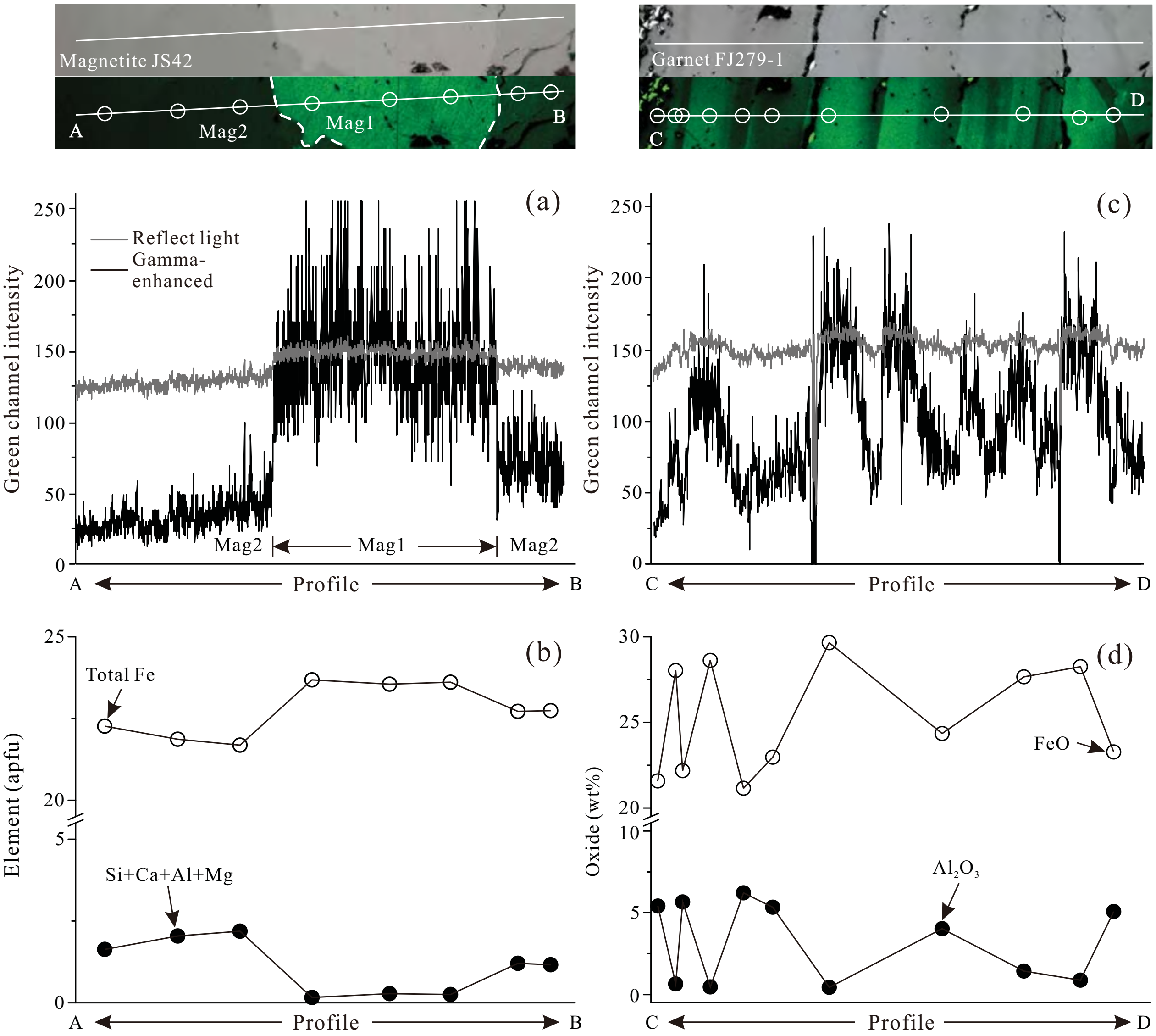
Magnetite JS42
A
Mag2
Mag1
B
Garnet FJ279-1
C
D
(a)
Reflect light
Gamma-enhanced
Green channel intensity
250
200
150
100
50
0
Mag2
Mag1
Mag2
A
Profile
B
(c)
C
Profile
D
(b)
Total Fe
Element (apfu)
25
20
5
0
Si+Ca+Al+Mg
A
Profile
B
(d)
Oxide (wt%)
30
25
20
10
5
0
FeO
Al_2O_3
C
Profile
D

Figure 6

Table 1. Electron microprobe data for magnetite（wt%）

Sample	Minimum detection limit	JS42 Y2-3-1										JS42 Z3-1				
		1	2	3	4	5	6	7	8	9	10	1	2	3	4	5
Sub-type		Mag2B	Mag2D	Mag2D	Mag1	Mag1	Mag1	Mag2B	Mag2B	Mag2B	Mag2D	Mag2D	Mag2B	Mag2D	Mag1	Mag1
SiO_2	0.03	2.52	3.01	2.98	<	<	0.09	1.99	1.97	2.43	3.45	3.43	2.16	3.24	0.05	<
TiO_2	0.11	<	<	<	0.27	0.27	0.25	<	<	<	<	<	<	<	<	0.12
Al_2O_3	0.02	0.98	1.23	1.32	0.30	0.53	0.41	0.69	0.73	0.89	1.45	1.61	0.89	1.34	0.33	0.30
V_2O_3	0.03	<	<	0.04	0.09	0.10	0.07	<	<	<	<	<	<	<	<	<
FeO*	0.05	61.20	60.26	60.65	68.49	68.37	68.04	64.38	63.12	62.10	58.96	57.35	62.15	58.94	68.05	68.29
Fe_2O_3*		32.10	32.45	32.11	31.09	31.08	31.13	32.48	32.31	32.61	33.53	32.04	32.02	32.87	30.73	30.90
MnO	0.05	0.22	0.18	0.14	0.12	0.17	0.15	0.21	0.15	0.16	0.18	0.10	0.16	0.15	0.13	0.12
MgO	0.03	0.44	0.80	1.14	0.12	0.20	0.16	0.28	0.14	0.23	0.45	1.07	0.34	0.51	0.07	0.06
CaO	0.02	0.95	1.04	1.00	<	<	<	0.74	0.73	0.96	1.14	1.04	0.86	1.13	<	<
CoO	0.04	0.10	0.06	0.14	0.17	0.13	0.08	0.09	0.14	0.13	0.10	0.13	0.10	0.11	0.12	0.09
Na_2O	0.02	0.10	0.14	0.22	<	0.04	0.03	<	0.13	0.10	0.15	0.15	0.16	0.13	0.07	<
K_2O	0.01	0.06	0.12	0.11	<	<	0.01	0.02	0.02	0.05	0.14	0.22	0.05	0.15	<	<
Total		98.65	99.28	99.87	100.64	100.89	100.42	100.88	99.44	99.65	99.56	97.12	98.89	98.55	99.54	99.87
Calculated based on 32 oxygen atoms																
Si		0.77	0.91	0.89	0.00	0.00	0.03	0.60	0.60	0.74	1.04	1.05	0.66	0.98	0.02	0.00
Ti		0.00	0.00	0.00	0.06	0.06	0.06	0.00	0.00	0.00	0.00	0.00	0.00	0.00	0.00	0.03
Al		0.35	0.44	0.47	0.11	0.19	0.15	0.24	0.26	0.32	0.51	0.58	0.32	0.48	0.12	0.11
V		0.00	0.00	0.01	0.02	0.03	0.02	0.00	0.00	0.00	0.00	0.00	0.00	0.00	0.03	0.02
Fe^{2+}		8.20	8.18	8.03	7.94	7.90	7.96	8.16	8.24	8.27	8.43	8.21	8.19	8.36	7.93	7.95
Fe^{3+}		14.07	13.68	13.65	15.74	15.65	15.65	14.56	14.50	14.17	13.34	13.23	14.30	13.48	15.80	15.81
Total Fe		22.27	21.87	21.69	23.68	23.55	23.61	22.72	22.74	22.44	21.77	21.44	22.49	21.84	23.73	23.76
Mn		0.06	0.04	0.04	0.03	0.04	0.04	0.05	0.04	0.04	0.05	0.03	0.04	0.04	0.04	0.03
Mg		0.20	0.36	0.51	0.05	0.09	0.07	0.13	0.06	0.10	0.20	0.49	0.15	0.23	0.03	0.03
Ca		0.31	0.34	0.32	0.00	0.00	0.00	0.24	0.24	0.31	0.37	0.34	0.28	0.37	0.00	0.00
Co		0.02	0.02	0.03	0.04	0.03	0.02	0.02	0.03	0.03	0.02	0.03	0.03	0.03	0.03	0.02
Na		0.01	0.02	0.03	0.00	0.01	0.00	0.00	0.02	0.01	0.02	0.02	0.02	0.02	0.01	0.00
K		0.01	0.01	0.01	0.00	0.00	0.00	0.00	0.00	0.00	0.01	0.02	0.00	0.01	0.00	0.00
Si+Ca+Al+Mg		1.63	2.04	2.19	0.16	0.28	0.25	1.21	1.16	1.47	2.12	2.46	1.42	2.06	0.17	0.14

Notes: Mag−magnetite; <−below minimum limit of detection;
* Signifies recalculated values based on 32 oxygen atoms.

Table 2. Electron microprobe data for garnet（wt%）

Sample	Minimum detection limit	FJ279-1 A2-1								FJ279-1 A2-2												
		1	2	3	4	5	6	7	8	1	2	3	4	5	6	7	8	9	10	11	12	13
Sub-type		Dark	Bright	Dark	Bright	Dark	Bright	Dark	Bright	Dark	Bright	Dark	Bright	Dark	Dark	Bright	Dark	Bright	Bright	Dark	Dark	Dark
SiO_2	0.03	36.33	35.45	36.63	35.07	36.08	35.01	37.12	35.12	36.71	35.13	35.83	35.19	36.22	36.13	34.99	36.42	35.36	35.53	36.51	35.85	37.48
TiO_2	0.03	0.59	0.04	0.40	0.04	0.16	<	0.19	<	0.56	0.03	0.52	<	0.44	0.61	<	<	<	0.04	0.04	0.08	0.04
Al_2O_3	0.02	5.86	0.68	5.43	0.53	6.13	1.97	5.62	0.39	5.41	0.65	5.66	0.47	6.22	5.34	0.44	4.03	1.43	0.88	5.01	5.01	6.36
Cr_2O_3	0.03	<	<	0.05	<	0.05	<	<	<	0.03	<	<	<	<	<	<	<	<	<	<	<	<
FeO	0.03	22.17	27.71	22.40	28.75	21.99	26.15	22.26	29.18	21.58	28.03	22.18	28.62	21.15	22.97	29.66	24.35	27.66	28.26	23.40	23.56	22.64
MnO	0.03	0.64	0.44	0.52	0.57	0.63	0.48	0.48	0.45	0.62	0.40	0.49	0.39	0.87	0.57	0.38	0.57	0.41	0.53	0.90	0.89	1.22
MgO	0.02		0.06	0.11	0.04	0.04	0.03	0.05	0.03	0.08	0.08	0.06		0.08	0.05	0.04	0.04					0.04
CaO	0.01	34.01	33.41	34.07	33.25	34.07	33.64	33.82	32.82	33.70	33.26	33.77	33.43	33.43	33.56	33.29	33.81	33.60	32.83	32.93	33.01	32.58
Na_2O	0.02	0.02	<	<	<	<	<	<	<	<	<	0.03	<	<	0.02	0.02	<	<	<	<	<	<
Total		99.62	97.78	99.60	98.25	99.15	97.28	99.54	97.98	98.69	97.58	98.54	98.10	98.42	99.24	98.81	99.22	98.47	98.06	98.79	98.39	100.35
End member (mol%)																						
Morimotoite								0.41		0.23												0.23
Spessartine								1.09		2.75				1.95	1.30				1.25	2.07	0.64	2.75
Almandine								1.63		4.25					0.02				0.04	1.67		4.25
Grossular		24.25	1.45	23.06		25.07	6.48	23.59		22.49	0.42	22.99		25.01	20.53		17.38	3.85	1.26	19.22	20.44	22.49
Andradite		71.88	96.84	73.72	97.29	71.67	90.93	72.30	98.01	68.95	97.38	73.54	97.75	70.44	74.81	96.79	80.91	93.83	96.16	76.18	75.92	68.95
Remainder		1.41	1.33	0.74	2.58	2.45	2.45	0.00	1.99	0.88	1.77	1.64	2.25	0.60	1.29	3.21	1.20	2.32	0.93	0.42	1.92	0.88

Notes: <—below minimum limit of detection.

Table 3. Electron microprobe data for wolframite（wt%）

Sample	Minimum detection limit	19XLK57 Y4-1					19XLK57 Y3-1					
		1	2	3	4	5	1	2	3	4	5	6
Sub-type		Wol2	Wol1	Wol2	Wol1	Wol2	Wol1	Wol2	Wol1	Wol2	Wol2	Wol1
FeO	0.07	15.25	10.17	14.83	4.99	12.64	5.83	10.24	4.37	9.31	10.50	5.37
MnO	0.07	9.22	13.39	8.97	18.76	11.59	17.36	13.18	18.81	12.85	13.37	18.04
WO_3	0.10	76.37	76.22	77.14	76.70	77.36	76.75	75.38	76.68	76.83	76.72	77.42
Total		100.84	99.81	100.99	100.46	101.60	99.96	98.82	99.88	99.00	100.62	100.86
Calculated based on 4 oxygen atoms												
Fe		0.64	0.43	0.62	0.21	0.53	0.24	0.43	0.18	0.39	0.44	0.22
Mn		0.39	0.57	0.38	0.80	0.49	0.74	0.56	0.80	0.54	0.57	0.76
W		0.99	0.99	1.00	0.99	1.00	1.00	0.98	0.99	1.00	1.00	1.00
End member (mol%)												
$MnWO_4$		37.97	57.14	37.99	79.21	48.15	75.11	56.59	81.33	58.29	56.34	77.30
$FeWO_4$		62.03	42.86	62.01	20.79	51.85	24.89	43.41	18.67	41.71	43.66	22.70

Notes: Wol−wolframite.

Table 4. Electron microprobe data for tetrahedrite-tennantite（wt%）

Sample	Minimum detection limit	JJW94 Z3-1							JJW94 Z3-2						
		1	2	3	4	5	6	7	1	2	3	4	5	6	7
Sub-type		Ttr	Ttr	Ten	Ten	Ttr	Ttr	Ten	Ten	Ttr	Ten	Ttr	Ten	Ten	Ttr
As	0.03	1.86	3.50	13.51	12.28	2.99	2.22	14.46	18.20	4.62	17.46	2.42	15.98	18.61	1.96
Zn	0.02	6.29	5.63	6.65	6.74	5.49	5.53	6.78	2.04	5.57	4.00	5.50	2.03	1.56	5.40
S	0.01	24.93	25.24	26.83	26.57	25.01	24.91	27.64	28.07	25.35	27.92	24.98	28.07	27.91	24.64
Pb	0.03	0.38	0.52	<	<	0.84	0.18	0.11	0.07	0.71	0.04	0.41	<	0.05	0.35
Bi	0.03	<	<	1.41	1.41	<	0.33	1.15	<	<	<	<	0.31	0.05	<
Sb	0.03	26.07	24.07	8.33	9.28	24.35	25.87	7.04	0.70	21.52	4.07	25.99	4.22	0.62	26.61
Ag	0.02	0.06	<	0.04	<	0.03	<	0.03	<	0.05	<	0.05	0.04	0.03	0.05
Cd	0.03	0.04	0.03	0.04	0.06	<	0.09	0.04	0.07	0.07	0.07	0.13	0.08	<	0.10
Cu	0.02	39.24	40.18	42.55	42.44	40.45	39.79	42.72	47.22	41.04	45.62	40.21	46.15	47.12	39.71
Fe	0.01	1.15	1.43	0.99	0.78	1.21	1.56	1.00	2.83	1.59	1.88	1.62	2.98	2.98	1.70
Total		100.02	100.61	100.35	99.56	100.37	100.50	100.96	99.20	100.52	101.08	101.31	99.86	98.94	100.53
Calculated based on 29 atoms															
Cu		10.21	10.31	10.32	10.41	10.45	10.31	10.19	11.05	10.44	10.67	10.34	10.88	11.07	10.33
Ag		0.01	-	0.01	-	0.00	-	0.00	-	0.01	-	0.01	0.00	0.00	0.01
Fe		0.34	0.42	0.27	0.22	0.36	0.46	0.27	0.75	0.46	0.50	0.47	0.80	0.80	0.50
Zn		1.59	1.40	1.57	1.61	1.38	1.39	1.57	0.46	1.38	0.91	1.37	0.46	0.36	1.37
Cd		0.01	0.00	0.00	0.01	-	0.01	0.01	0.01	0.01	0.01	0.02	0.01	-	0.02
As		0.41	0.76	2.78	2.55	0.66	0.49	2.93	3.61	1.00	3.46	0.53	3.19	3.71	0.43
Sb		3.54	3.22	1.05	1.19	3.28	3.50	0.88	0.08	2.86	0.50	3.49	0.52	0.08	3.61
Bi		-	-	0.10	0.11	-	0.03	0.08	-	-	-	-	0.02	0.00	0.00
Pb		0.03	0.04	-	-	0.07	0.01	0.01	0.01	0.06	0.00	0.03	-	0.00	0.03
S		12.86	12.84	12.89	12.91	12.81	12.79	13.07	13.02	12.79	12.95	12.73	13.11	12.99	12.70

Notes: Ttr−Tetrahedrite; Ten−tennantite; <−below minimum limit of detection.

Table 5. Element substitution induced increase/decrease of reflectance for Fe-bearing minerals

Mineral	Formula	Reflectance (%)	Increase of reflectance	Decrease of reflectance	References
Magnetite	$FeFe_2O_4$	20–21		Si^{4+} (Fe^{3+}), Al^{3+} (Fe^{3+}), Ca^{2+} (Fe^{2+}), Mg^{2+} (Fe^{2+})	Criddle and Stanley 1993; This study
Garnet (andradite-grossular series)	Ca_3 (Fe, Al)$_2$ Si_3O_{12}	~9 for andradite	Fe^{3+} (Al^{3+})		This study
Wolframite	(Fe, Mn) WO_4	15~16 for huebnerite	Fe^{2+} (Mn^{2+})		This study
Tetrahedrite-tennantite	$Cu_6(Cu_4(Fe, Zn)_2)(Sb, As)_4S_{13}$	31–33	Fe^{3+} (Cu^{2+}), Zn^{2+} (Cu^{2+}), Ag^+ (Cu^+)	As^{3+} (Sb^{3+})	Hall et al. 1974, This study
Pyrite	FeS_2	36–55		As^{3+} (Fe^{2+}), As^{1-} (S_2^{2-}), Co^{2+} (Fe^{2+}), Ni^{2+} (Fe^{2+})	Vaughan 1969; Zhu et al. 2021
Sphalerite	ZnS	16–17	Fe^{2+} (Zn^{2+})		Awadh 2009; Lai et al., 2023
Chromite	$FeCr_2O_4$	13–17	Fe^{3+} (Cr^{3+})	Al^{3+} (Cr^{3+})	Eales 1980; López-Benito et al. 2017
Goethite	FeO(OH)	15–17		Si^{4+} (Fe^{3+}), Al^{3+} (Fe^{3+})	Donskoi et al. 2022
Ilmenite	$FeTiO_3$	17–20		Mg^{2+} (Fe^{2+})	Cervelle et al. 1971

Note: reflectance values of minerals (at 589 nm in air) are from Criddle and Stanley (1993) and Stanley (2013); elements in brackets were replaced by elements outside.